Direct Observation of Early-Time Hydrogelation in β-Hairpin Peptide Self-Assembly

Tuna Yucel,[†,‡] Chris M. Micklitsch,[§,⊥] Joel P. Schneider,[*,§] and Darrin J. Pochan[*,†,‡]

Department of Materials Science and Engineering, Delaware Biotechnology Institute, and Department of Chemistry and Biochemistry, University of Delaware, Newark, Delaware 19716

Received December 20, 2007; Revised Manuscript Received April 21, 2008

ABSTRACT: Triggered hydrogelation of MAX1 peptide, $(VK)_4$-V^DPPT-$(KV)_4$-NH_2, proceeds through peptide intramolecular folding into β-hairpins and concomitant self-assembly into branched clusters of well-defined (uniform, 3 nm cross section), semiflexible, β-sheet-rich nanofibrils. Cryogenic transmission electron microscopy indicates that dangling fibrils extend from one growing cluster to another and lead to early, intercluster communication in solution. At the apparent percolation threshold, the dynamic shear modulus measured by oscillatory rheology ($G'(\omega)$, $G''(\omega) \propto \omega^n$) and the field-intensity autocorrelation function measured by dynamic light scattering ($g_1(\tau) \propto \tau^{-\beta'}$) show power-law behavior with comparable critical dynamic exponents ($n \approx 0.47$ and $\beta' \approx 0.45$). Finite interpenetration of percolating clusters with smaller clusters, along with permanent intercluster entanglements, increase the network rigidity. The self-assembly of MAX1 peptide was compared and contrasted with the assembly of other biopolymeric networks in literature.

1. Introduction

Stimuli-responsive hydrogels show promise for use as biomaterials, e.g., in tissue engineering,[1–3] microfluidics,[4,5] and drug delivery.[6–8] We have previously presented a peptide that undergoes intermolecular self-assembly into hydrogel scaffolds following an intramolecular folding event. This intramolecular folding event can be triggered by solution stimuli such as changes in pH,[9] temperature,[10] ionic strength,[11–13] photoinitiation,[14] or the introduction of cell culture media.[15] Notably, the gelation kinetics and overall gel mechanical properties can be controlled precisely by choosing the desired type and magnitude of stimulus[11] and by manipulating the peptide design.[16] Recently, the gelation kinetics were directly correlated with changes in molecular conformation of the peptide.[17] In the present paper, we present a detailed, nanoscopic through microscopic picture of the evolution of self-assembled structure toward formation of a percolated hydrogel network.

The growth mechanism of fibrillar biopolymer networks, such as sickle cell hemoglobin (s-hemoglobin)[18] and collagen type I,[19] has been studied extensively. In these systems, self-assembly starts with nucleation of individual fibrils. This homogeneous nucleation is followed by heterogeneous nucleation of new fibrils alongside pre-existing ones, leading to both thickening along a fibril and branching into clusters. Eventually, clusters interconnect and interpenetrate to give elastic-like behavior. The interest in the structural aspects of natural systems stems from possible relationships between the assembly mechanisms, the kinetics of assembly, the local fibrillar and global cluster morphology, and final material properties. For example, a strong correlation was observed between the self-assembled structure and the assembly kinetics of s-hemoglobin.[20] It was proposed that the branching of s-hemoglobin fibrils defines the autocatalytic growth in this system, as described by a double nucleation model. Therefore, structural aspects such as fibril branching may define the assembly kinetics as in the s-hemoglobin example. Previous work from our laboratory[12,13] and recent simulations of Douglas and co-workers on molecular self-organization into one-dimensional chains[21] suggest that the reverse may also be true, i.e., assembly kinetics may effectively dictate the self-assembled structure; specifically, deeper quench depths/faster assembly kinetics have been observed both experimentally[12,13] and by simulations[21] to lead to a higher density of self-assembled branches. As emphasized by deGennes[22] and others,[23] even a low concentration of such branches can significantly affect the dynamic properties of a chain system, e.g., chain reptation can be quenched by just a few branches along the chain. Therefore, direct observation of such self-assembled structural features like fibril branching is essential to the understanding of final self-assembled material properties.

The characterization of the early-time β-hairpin assembly has potential biotechnological importance in the design of injectable hydrogels for in vivo tissue regeneration.[16] For example, β-hairpin self-assembly and hydrogelation can be triggered in cell culture medium, leading to well-controlled, homogeneous, three-dimensional encapsulation of a desired cell type at a desired cell density.[16] These solid cell−gel constructs shear thin on application of stress, such as during injection from a syringe, to a targeted, in vivo site. Importantly, the stiffness of the network recovers immediately when the applied stress is removed (i.e., after injection from a syringe has stopped[11,16]). Therefore, it is important to understand the initial gelation of the peptides in order to directly observe the pathway through which the hydrogel network first interacts with suspended cells, allowing potential cytocompatibility−self-assembly relationships to be observed.

We previously presented a peptide design that related the stimuli-responsive, intramolecular folded state of the peptide to its tendency to intermolecularly self-assemble and form hydrogels.[9–17] The design of MAX1, a 20-residue peptide, included alternating hydrophobic valine and hydrophilic lysine groups to promote β-sheet formation, flanking a tetrapeptide turn sequence (MAX1: $(VK)_4$-V^DPPT-$(KV)_4$-NH_2). Figure 1a summarizes the self-assembly mechanism proposed for MAX1 peptide. Under low to neutral pH solution conditions positively charged lysine residues preclude peptide intramolecular folding. However, the β-hairpin folded state can be attained by deprotonating[9] or screening[11] the charges on lysine side chains (Figure

* Corresponding authors: e-mail schneijp@udel.edu, Ph (302)831-3024 (J.P.S.); e-mail Pochan@udel.edu, Ph (302)831-3567, fax (302)831-4545 (D.J.P.).
† Department of Materials Science and Engineering.
‡ Delaware Biotechnology Institute.
§ Department of Chemistry and Biochemistry.
⊥ Current address: Laboratory of Bioorganic Chemistry, National Institutes of Health, Bethesda, MD 20892.

10.1021/ma702840q CCC: $40.75
Published on Web 07/01/2008

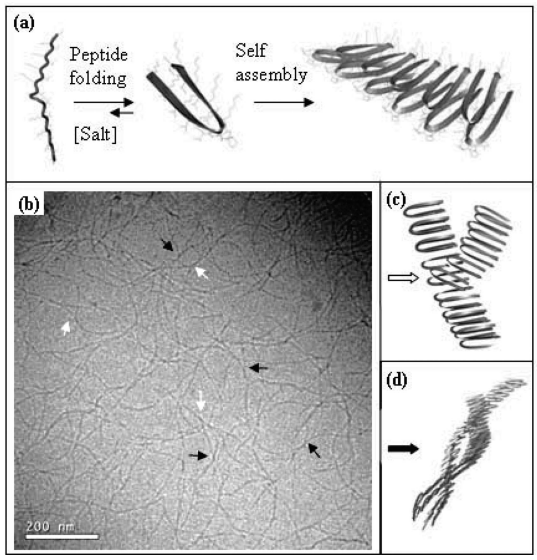

Figure 1. (a) Proposed self-assembly mechanism when folding is triggered by increasing the solution ionic strength,[9] and (b) in situ observation of the hydrogel network by cryo-TEM. The arrows in (b) indicate two different self-assembled cross-links: defect-induced branch (white) and entanglement (black). Schematic representations in (c) and (d) show a defect-induced branch and an entanglement, respectively.

1a shows the folding stimulus used in this paper, i.e., increasing the salt concentration) or through enhancement of the hydrophobic effect of the valine side chains.[10] In the folded state intramolecular hydrogen bonds are formed. Once folded into a β-hairpin, the peptide becomes facially amphiphilic and self-assembles both facially through hydrophobic association and laterally, primarily via intermolecular hydrogen bonding, into bilayered β-sheet fibrils with a hydrophobic core. These well-defined, bilayered fibrils form β-sheet-rich hydrogel networks. Considering the peptide molecular design and the proposed self-assembly mechanism, possible physical cross-linking mechanisms include (1) self-assembly defect-induced branching (Figure 1c)[24] and (2) entanglement of self-assembled fibrils (Figure 1d). In defect-induced branching, kinetically trapped, imperfect valine-face hydrophobic collapse may lead to nucleation of a branch (Figure 1c). Both defect-induced branching and entanglements can behave as permanent physical cross-links. The gelation kinetics of MAX1 can be controlled precisely by changing the assembly conditions, e.g., by altering the ionic strength and/or temperature of assembly.[11] Specifically, faster assembly kinetics due to a larger magnitude of folding stimulus, such as high salt concentration leading to more significant screening of lysine interactions or higher temperatures leading to more significant hydrophobic interactions, normally leads to stiffer gels. However, a detailed analysis of assembly kinetics has not yet been presented. Likewise, the structural aspects that dominate the dependence of network mechanical properties on the magnitude of solution stimulus should be identified. For example, the dependence of network rigidity on assembly temperature can be due to changes in single fibril dynamics and/or the nature, strength, concentration, and spatial distribution of junctions formed at different assembly temperatures. Here, we present a study on the early time growth mechanism, from the triggering of peptide intramolecular folding to hydrogel network percolation, of β-hairpin self-assembly and present a basis for physical characterization aimed at the isolation of the factors most significant in controlling the stimuli-triggered, self-assembly dictated mechanical properties.

Previously, a gel point of β-hairpin self-assembly was estimated, under slow assembly conditions using microrheology, which was correlated with the β-sheet content in the system.[17] Here, we study the different stages of the evolution of the network structure directly and, in the case of cryo-TEM, in situ without any extraneous agents or probes. As such, the noted manipulation of assembly kinetics by possible peptide−probe interactions was prevented and an overall picture of the nanostructural growth due to peptide intramolecular folding and intermolecular self-assembly was obtained. In order to comprehensively characterize the early time self-assembly and gelation behavior, we took advantage of the stimuli responsiveness of folding and self-assembly. We adjusted the solution conditions to enable direct comparison between circular dichroism (CD) spectroscopy, dynamic light scattering (DLS), small-angle neutron scattering (SANS), cryogenic transmission electron microscopy (cryo-TEM), and oscillatory rheology data acquired on the same peptide system at the same time points. CD monitored the changes in molecular conformation (from random-coil to β-sheet) during folding and self-assembly. Cryo-TEM enabled direct observation of nanostructure growth through intermolecular self-assembly which was confirmed by the SANS data. Rheology observed changes in viscoelastic properties associated with percolation and gelation of growing fibril nano- through microstructure. DLS detected changes in dynamic density fluctuations due to early fibril and cluster growth and formation of static inhomogeneities due to gelation. As such, a direct observation of structure evolution was correlated with changes in hydrogel rigidity. Ultimately, the goal is to be able to correlate the hydrogel structural growth mechanism with observed mechanical properties and biological properties such as in vitro cell function and response. We believe that a thorough understanding of structure evolution and assembly kinetics will be necessary for future peptide design for biological applications as well as for realization of new peptide engineering opportunities.

2. Experimental Section

2.1. Sample Preparation. MAX1 was synthesized on amide resin via automated Fmoc-based solid-phase peptide synthesis employing an ABI 433A peptide synthesizer and HBTU/HOBT activation. The details of the peptide synthesis are given elsewhere.[9] Hydrogels were prepared by first preparing a stock solution of the lyophilized peptide in DI water and then adjusting the desired final solution conditions by the subsequent addition of an equal volume of buffer solution. In particular, peptide concentration, solution pH, monovalent salt concentration, and temperature were set at 0.75 mM (0.25 wt %) MAX1 peptide, pH 7.0 (50 mM bis-tris propane buffer), 0.4 M salt, and 22 °C, respectively (termed "high salt" for the remainder of the paper). This buffer and salt concentration lead to a Debye screening length,[25] κ^{-1}, of ~0.5 nm. The high salt assembly condition was chosen so that the initial self-assembly into solid hydrogel took more than 1 h. This hydrogelation time allowed different experimental techniques to be performed under the same assembly conditions and same time points so that different stages of self-assembly could be resolved. In addition, a control solution condition was identified for which neither a change in the initial molecular conformation nor a change in nanostructure attributable to self-assembly was detected. Data collected under the control solution condition both highlighted the strong folding stimulus responsiveness of the assembly process and confirmed that the observed changes in the system related directly to the self-assembly process and were not simply due to possible artifacts caused by changes in instrument stability or other effects such as degradation of sample over the observed period. For the control experiments, all solution conditions were kept the same as those for the high salt condition, except the salt concentration was lowered to 0.05 M (termed "low salt" from now on) to obtain $\kappa^{-1} \approx 1$ nm. NaCl was used to increase the solution salt concentration for all experiments except circular dichroism (CD) spectroscopy. For CD experiments KF salt was used to minimize the UV absorption of the sample. The substitution of salt did not affect the assembly

kinetics as observed by time evolution of DLS count rates. For SANS experiments, peptide stock solution and the buffers were prepared in D_2O. Zero time in each experiment was taken as the time at which the buffer solution was added to the peptide stock solution.

2.2. Circular Dichroism Spectroscopy. Circular dichroism (CD) spectra were collected using a Jasco J-810 spectropolarimeter. The peptide solutions in buffer were kept in ice-cold water to suppress folding and self-assembly, and samples were immediately loaded in a 0.1 mm quartz cell. Wavelength scans were collected continuously between 190 and 260 nm after raising the temperature to 22 °C to observe the time dependence of the CD signal. The data collection time for each spectrum was 104 s. The mean residue ellipticity, $[\theta] = \theta_{obs}/10lcr$, where θ_{obs} is the difference between the ellipticity values measured from the sample and the values measured from the buffer solution without peptide in millidegrees, l is the path length of the cell in centimeters, c is the molar peptide concentration, and r is the number of residues.

2.3. Cryogenic Transmission Electron Microscopy. Buffered peptide solutions were kept in the temperature- and humidity-controlled chamber of the Vitrobot (FEI Co.) at 22 °C and 100% humidity for predetermined times to allow self-assembly to occur. At each time point of interest, 3 μL of peptide solution was applied onto copper TEM grids coated with lacey carbon support films (Electron Microscopy Sciences). After application of the sample on the grid, the solutions were allowed to relax for 10 s, and excessive sample was blotted away using filter paper. The remaining thin layer of sample was again allowed to relax for 10 s under controlled atmosphere and subsequently plunged into liquid ethane kept at $T = -170$ °C to ensure complete sample vitrification. Vitrified samples were transferred into a Gatan cryo-transfer holder in liquid nitrogen. A Tecnai G2 12 twin transmission electron microscope equipped with a low-dose CCD camera was used at 120 kV accelerating voltage to image the samples. During imaging the temperature of the holder was maintained below $T = -170$ °C to prevent sublimation and crystallization of vitreous water.

2.4. Small-Angle Neutron Scattering. SANS experiments were performed on the 30 m instrument on beamline NG3 at the National Center for Neutron Research (NCNR), National Institute of Standards and Technology (NIST), Gaithersburg, MD. The neutron beam was monochromated to a wavelength $\lambda = 9$ Å with a velocity selector having a wavelength spread $\Delta\lambda/\lambda = 0.15$. The scattered neutrons were detected by a 64 cm × 64 cm two-dimensional detector using three different sample-to-detector distances of 13, 4, and 1.3 m. These configurations allowed values of the scattering wavevector, $q = (4\pi/\lambda)\sin(\theta/2)$, where θ is the scattering angle, in the range $0.004\ \text{Å}^{-1} < q < 0.500\ \text{Å}^{-1}$. The resulting data were corrected for background electronic noise, detector inhomogeneity, empty cell scattering, and solvent scattering. The uncertainties of the $I(q)$ vs q individual data points were calculated statistically from the number of averaged detector counts. SANS data were analyzed using models that are available from NCNR at NIST (cylindrical form factor fits[26] and a modified Guinier analysis for a rod[12,27]). In the modified Guinier analysis for a rod-like scatterer, the form factor $P(q) \propto (1/q)\exp[(-q^2R_{GC}^2)/2]$, where R_{GC} is the cross-sectional radius of gyration. Therefore, the slope of the scattering data plotted as $\ln[qI(q)]$ vs q^2 gives $-R_{GC}^2/2$, and the rod cross section, $r = R_{GC}\sqrt{2}$.

2.5. Dynamic Oscillatory Rheology. Dynamic oscillatory time, frequency, and strain sweeps were performed using an AR2000 stress-controlled rheometer (TA Instruments) with 25 mm diameter parallel plate geometry at 0.5 mm measuring gap distance. Custom-made, borosilicate glass disks were attached on both the bottom and top plates of the rheometer. These attachments were plasma cleaned immediately before each experiment to render the surfaces hydrophilic and prevent heterogeneous nucleation from the plate surfaces. Buffered peptide solutions were kept in ice-cold water before loading onto the rheometer plate to suppress folding and self-assembly. The top plate was lowered to the desired gap distance, and the buffered peptide solutions were applied via syringes. Either a NIST traceable standard low-viscosity mineral oil (Cannon Instruments, S3, kinematic viscosity, $\eta \approx 3$ mPa·s at 22 °C) or a high-viscosity, siloxane-based oil (Degussa-Goldschmidt, ABIL EM90, $\eta \approx 2$ Pa·s at 22 °C) was used to prevent sample evaporation from the sides of the plate. Dynamic oscillatory time sweeps were collected at multiple angular frequencies ($\omega = 1-100$ rad s^{-1}) simultaneously in order to probe the time progress of the frequency response. The frequency range was selected so that the duration of each frequency sweep was much shorter than time scales relevant to the assembly process. At the end of each experiment, a frequency sweep was collected over a wider range of ω values ($\omega = 0.1-100$ rad s^{-1}). To ensure that the strain applied during rheological testing did not affect MAX1 peptide self-assembly, we carried out control experiments at different strain amplitudes. The time evolution of the mechanical response for the high salt condition was not affected by strain amplitude from $\gamma = 1\%$ up to $\gamma = 10\%$ (Figure SI-1). Therefore, possible effects of strain on structure could be ignored up to $\gamma = 10\%$ for the purpose of this paper. Strain sweep measurements were performed from 0.01 to 1000% strain at the end of each experiment to determine the linear viscoelastic regime of the final hydrogel.

2.6. Dynamic Light Scattering. For dynamic light scattering (DLS) experiments, chilled, aqueous peptide stock solution and the buffer stock solution were separately filtered into 1.2 cm outer diameter glass cells. After gentle mixing, samples were loaded in the thermostated cell compartment of a Brookhaven Instruments BI200-SM goniometer equipped with a diode laser operated at a wavelength $\lambda = 532$ nm. The temperature was controlled with 0.05 °C accuracy with a thermostated recirculating bath. Scattered light intensity at 90°, $I_{90°}$, and the time-averaged autocorrelation function (ACF) of the scattered intensity, $g_2(q,t)$, were measured simultaneously using a Brookhaven BI-9000 correlator. The relaxation of density fluctuations at wave vector q and time t is probed from $g_2(q,t) = \langle I(t)I(0)\rangle/\langle I\rangle^2$, where q is related to the refractive index of the solvent n by $q = (4\pi n/\lambda)\sin(\theta/2)$. When the system is *ergodic*, i.e., when a time-averaged measurement of a property gives a good estimate of its ensemble average, $g_2(t)$ is related to the normalized field correlation function, $g_1(q,t)$ by the Siegert relation:[28]

$$g_2(q,t) = 1 + A^2 g_1(q,t)^2 \tag{1}$$

where A is the instrumental coherence factor. Equation 1 is not valid when the motion of scatterers is limited, e.g., due to gelation. When a solution turns into a gel, density fluctuations in solution can essentially freeze and turn into rather static concentration fluctuations of the gel network.[29] Such static components can act as scattering centers within the gel and cause multiple scattering or *homodyning*. A typical result of homodyning is a decrease in the initial, short delay time amplitude of the autocorrelation function. Therefore, we used Williams−Watts and CONTIN methods to analyze the mean and the distribution of relaxation times in the self-beating mode, only when there was no detectable homodyning. In the Williams−Watts or stretched exponential method, $g_1(t)$ is approximated by the expression

$$g_1(t) = \exp\left(-\left(\frac{t}{\tau_w}\right)^{\beta}\right) \tag{2}$$

where $\tau_w$localizes the position of the relaxation peak and β is the peak width. The mean relaxation time $\langle\tau_R\rangle$ can be calculated from τ_w and β by $\langle\tau_R\rangle = (\tau_w/\beta)\Gamma(1/\beta)$, where Γ is the gamma function. If several relaxation times, $\tau_{R,i}$, are present in a system, then $g_1(q,t)$ is given by an integral of the form $g_1(t) = \int\omega(\tau_R)\exp(-t/\tau)\,d\tau$, where $\omega(\tau_R)$ is a continuous function of relaxation times. Thus, $g_1(t)$ is related to $\omega(\tau_R)$ by a Laplace transformation. One of the most common methods used to invert this Laplace transformation and obtain the distribution of relaxation times from the measured $g_2(t)$ is the CONTIN regularization algorithm encoded by Provencher.[30] In CONTIN analysis, the position and the amplitude of the calculated relaxation time distributions show a weak dependence on data smoothing using the regularization parameter, while the width of the distributions may vary considerably.[31] Therefore, the distribution of relaxation

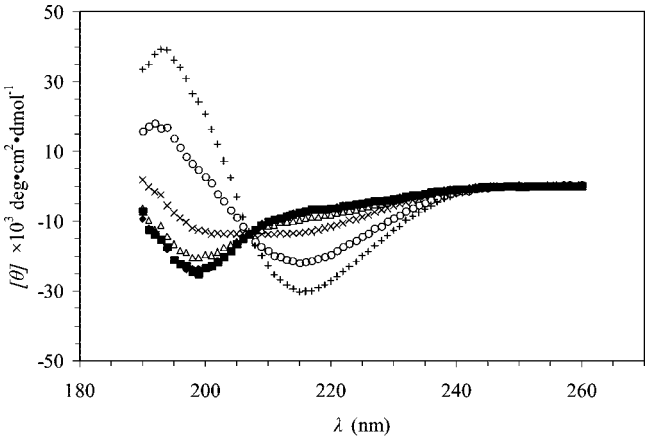

Figure 2. CD wavelength scans collected for two assembly conditions at different time points after the addition of buffer solution: (Δ) $t = 4$ min, (×) $t = 9$ min, (○) $t = 30$ min, and (+) $t = 306$ min for the high salt sample and (■) $t = 8$ min and (◆) $t = 458$ min for low salt control.

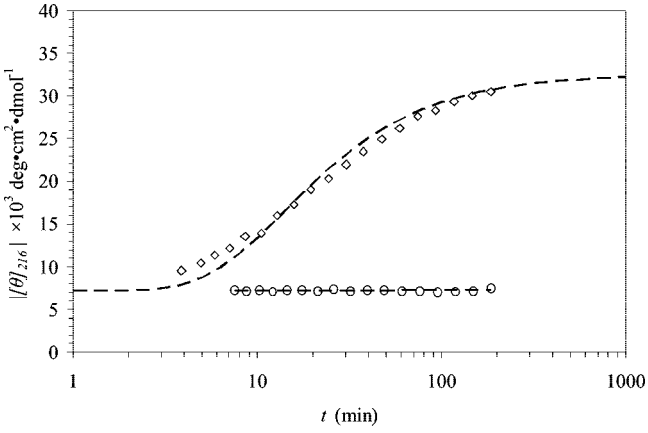

Figure 3. Time evolution of $|[\theta_{216}]|$ signal for the high salt sample (◇) and low salt control (○).

times obtained by CONTIN analysis should be considered semi-quantitative.

3. Results

Exploiting the previously demonstrated stimuli responsiveness of MAX1 self-assembly,[9–15] the assembly conditions (peptide concentration, solution pH, temperature, and ionic strength) were adjusted to obtain desired assembly kinetics that facilitated direct comparison between data collected by different techniques under the same, high salt assembly conditions. For control experiments, a low salt buffer was used. The specifics of the high salt assembly and low salt control conditions were given in subsection 2.1.

3.1. Circular Dichroism Spectroscopy. The addition of high salt buffer to the peptide solution to obtain $\kappa^{-1} \approx 0.5$ nm led to a transition from a secondary structure that was initially rich in random coil content to that rich in β-sheet (Figure 2). A control peptide solution in a low salt buffer ($\kappa^{-1} \approx 1$ nm) did not lead to any detectable change in the CD signal over the observed period, indicating that the forces dictating self-assembly operate in subnanometer length scales (0.5−1 nm). For the high salt sample, the mean residue ellipticity at 216 nm ($[\theta_{216}]$), which is indicative of the β-sheet content in the system, increased while the rate of increase of $|[\theta_{216}]|$ decreased with time and $[\theta_{216}]$ approached a plateau value, $[\theta_{216}]_\infty$ (Figure 3). The time evolution of $[\theta_{216}]$ signal could be modeled by an equation of the form $[\theta_{216}](t) = [\theta_{216}]_\infty \exp(-B/t)) + [\theta_{216}]_0$, where B is an arbitrary constant and $[\theta_{216}]_0$ is the zero-time value ($[\theta_{216}]_\infty$ and $[\theta_{216}]_0$ were -3.3×10^4 and -7.5×10^3 deg cm^2 dmol^{-1}, respectively). Both peptide intramolecular folding and subsequent intermolecular self-assembly lead to an increase in β-sheet signal due to the intramolecular and intermolecular hydrogen bonding associated with each assembly step. Therefore, changes in secondary structure observed by CD are evidence for both folding and self-assembly. We could estimate the extent of β-sheet formation, X_A, by $X_A = ([\theta_{216}](t) - [\theta_{216}]_0)/([\theta_{216}]_\infty - [\theta_{216}]_0)$. In order to gain more complete insight directly concerning self-assembly, CD was coupled with data on structural growth from cryo-TEM and scattering experiments.

3.2. Cryogenic Transmission Electron Microscopy and Small-Angle Neutron Scattering. The slow assembly kinetics for low peptide concentrations (0.25 wt %) under high salt conditions ($\kappa^{-1} \approx 0.5$ nm) afforded direct observation of in situ structure evolution by cryo-TEM. Cryo-TEM prevents possible artifacts such as microstructural rearrangement, composition changes, or drying stresses that may occur during conventional TEM sample preparation techniques (e.g., fixation, staining, and drying). In cryo-TEM,[32–34] the sample is directly vitrified in a cryogenic liquid and imaged without further processing. To the best of our knowledge, we are presenting the first study on direct, in situ observation of the early stages of hydrogelation of a designed peptide using cryo-TEM.

Figure 4 shows cryo-TEM micrographs collected at different, subsequent aging times. The earliest discernible structures were several hundred nanometer long, self-assembled nanofibrils observed at $t = 10$ min as dark lines on the light background of vitrified water (Figure 4a). Fibril cross section, d, was measured from cryo-TEM images as $d = 3 \pm 0.5$ nm and remained constant throughout the observed period. This observation is in good agreement with the proposed self-assembly mechanism[9] starting from the earliest stages of assembly observable by cryo-TEM, as described in Figure 1 and as verified by small-angle neutron scattering (SANS) (Figure 5). The scattered intensity in the intermediate q regime, $I(q) \propto q^{-1}$, as expected for scattering from a solution of rigid-rod-like objects. The d value was calculated as $d \approx 3$ nm using a modified Guinier analysis (see section 2.4 for a more detailed discussion) (Figure 5 inset), in very good agreement with d values measured from cryo-TEM images. Fibrils formed trifunctional (Figure 4b) and tetrafunctional junctions or branch points (Figure 4c). Junctions in MAX1 fibrils morphologically resemble those in cylindrical micelles forming branched networks[35,36] and large ovalbumin aggregates.[37] These junctions may result from self-assembly defects;[24] i.e., junctions may form through imperfect facial collapse of β-hairpin valine faces that causes nucleation of a branch from exposed hydrophobic groups. Tri- or tetrafunctional branch points observed by cryo-TEM presumably formed with this mechanism, since there is no difference in contrast between the rest of the fibril and the junction point. If the junction had formed due to an entanglement of two fibrils, we would expect twice the contrast at the junction due to the two cross sections of fibril through which the electrons must pass as compared to the single fibril cross section of a branch point. Here, we should note that the defect induced cross-linking mechanism is distinct from the heterogeneous nucleation model proposed for s-hemoglobin polymerization.[18] In the heterogeneous nucleation model a branch can form anywhere along a pre-existing fibril. However, defect-induced branching can only nucleate from a valine face collapse imperfection site (Figure 1c). In addition to distinct junctions, clusters of fibrils (or self-assembly mutants following the nomenclature by Douglas et al.[21]) were also observed at $t = 10$ min (Figure 4d).

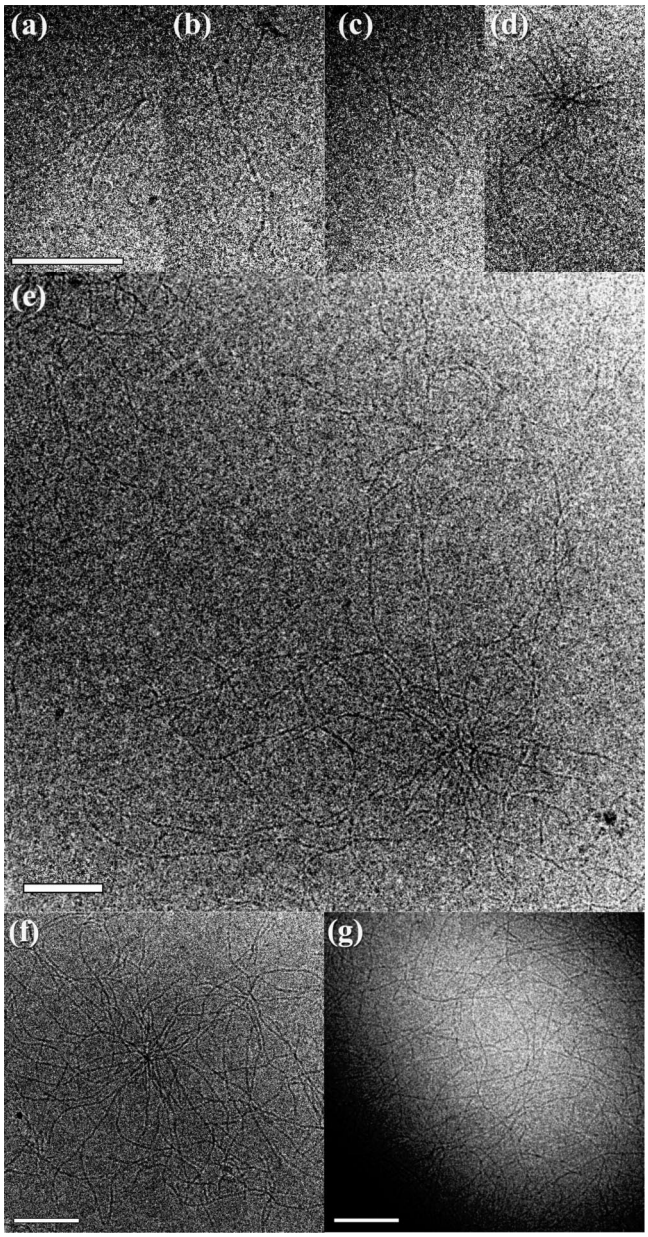

Figure 4. Cryo-TEM images showing different steps in formation of the hydrogel network: (a−d) $t = 10$ min, (e, f) $t = 26$ min, and (g) $t = 45$ min (scale bars represent 200 nm).

An overall growth of the fibril clusters was observed at $t = 26$ min (Figure 4e). The spacing between clusters was qualitatively comparable to the cluster size, indicating possible intercluster interactions in solution through dangling fibrils that extended from one cluster to another. Higher order branching was visible within the clusters (Figure 4f). At $t = 45$ min (Figure 4g), cluster sizes were on the order of micrometers and apparently interpenetrated with neighbors. This indicated an approach to an infinite percolating cluster. The images collected at $t = 45$ min were indistinguishable from those collected from later time gel samples due to the high concentration of fibrils. In brief, cryo-TEM suggests that peptides immediately began to fold and self-assemble into fibrillar nanostructures that elongated and branched to form fibril clusters. These pregel clusters could apparently physically interact in solution through dangling fibrils at $t \approx 26$ min while the clusters extended over several micrometers and seemed to begin to interpenetrate at $t \approx 45$ min. It was not possible to detect an exact gelation threshold solely by cryo-TEM morphology characterization. To investigate possible critical behavior associated with gelation, we combined CD and cryo-TEM with dynamic oscillatory rheology and dynamic light scattering.

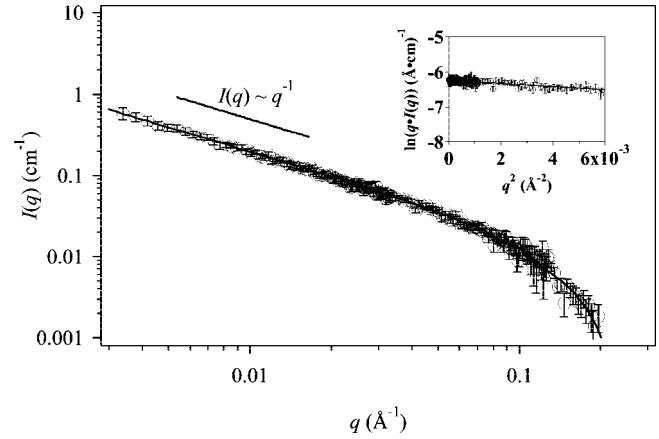

Figure 5. SANS data collected from the high salt sample at $t = 45$ min. The inset shows the modified Guinier analysis of $t = 45$ min data.

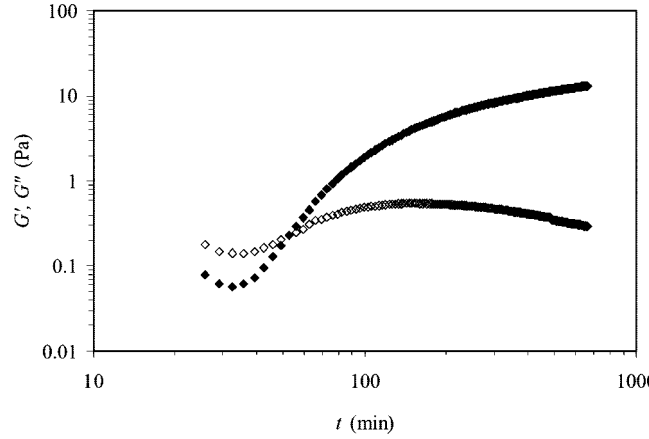

Figure 6. Dynamic oscillatory rheology time sweep data collected at $\omega = 1$ rad s^{-1} and $\gamma = 10\%$ (G': solid symbols; G'': open symbols).

3.3. Rheology. Dynamic oscillatory time sweep data were collected under the same, high salt assembly condition that was used for CD and cryo-TEM experiments. Data at multiple frequencies were collected simultaneously in the angular frequency range $\omega = 1-100$ rad s^{-1}. The slow assembly kinetics ensured that the system remained relatively unchanged during each frequency sweep. However, because G' is concentration dependent and very low peptide concentration (0.25 wt %) must be used to achieve such slow assembly kinetics, the final hydrogel rigidity was low ($G' \approx 20$ Pa).

Figure 6 shows the temporal progress of the dynamic oscillatory shear moduli collected at $\omega = 1$ rad s^{-1}. The measured response was initially that of a low viscosity liquid with $G'' > G'$, where G'' is the loss modulus and G' is the storage modulus. We observed a G', G'' crossover at $t \approx 50$ min for $\omega = 1$ rad s^{-1}. Chambon and Winter proposed that the loss tangent, tan δ, is frequency independent (tan $\delta(\omega) =$ tan $\delta(\omega)_c = G'(\omega_c)/G''(\omega_c) =$ constant, where subscript c denotes a critical value) for a "critical" gel,[38] i.e., when an incipient, infinite percolating cluster first spans the whole sample volume. For tan δ_c to be frequency independent, G' and G'' should have the same, power-law frequency dependence ($G'(\omega)_c$, $G''(\omega)_c \propto \omega^n$), where tan δ_c is related to the critical dynamic exponent n by tan $\delta_c = \tan(n\pi/2)$.[38] The power-law behavior of dynamic moduli is commonly attributed to the self-similarity of a "critical" gel at the length scales corresponding to the frequen-

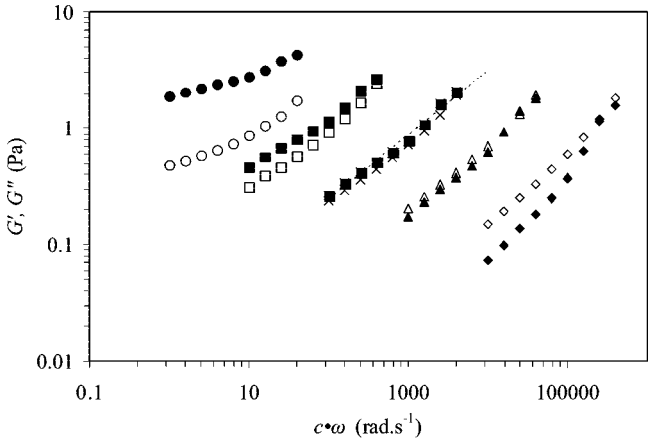

Figure 7. Dynamic oscillatory rheology frequency sweep data collected at different time points ($\gamma = 10\%$): (◇) $t = 40$ min ($c = 10^4$), (Δ) $t = 50$ min ($c = 10^3$), (×) $t = 56$ min ($c = 10^2$), (□) $t = 63$ min ($c = 10^1$), and (○) $t = 100$ min ($c = 10^0$), where c is an arbitrary shift factor used for easy visualization of multiple frequency sweeps (G': solid symbols; G'': open symbols).

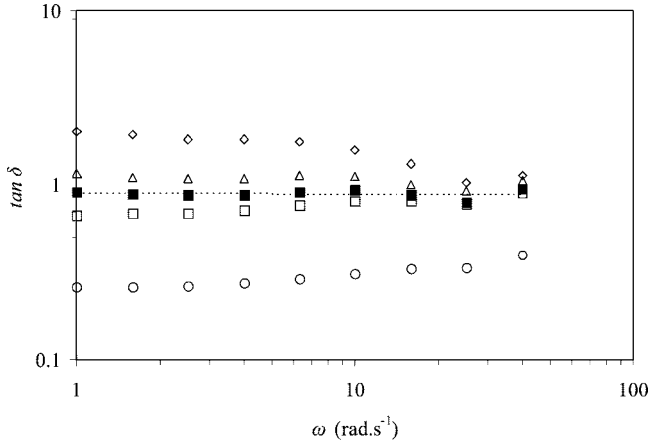

Figure 8. Frequency dependence of the loss tangent at different time points ($\gamma = 10\%$): (◇) $t = 40$ min, (Δ) $t = 50$ min, (■) $t = 56$ min, (□) $t = 63$ min, and (○) $t = 100$ min.

cies probed by rheology.[38,39] To investigate a possible gelation threshold as defined by Chambon and Winter, we observed the time evolution of the frequency response (Figure 7). For $t <$ 50 min, G'' was greater than G' at all measured frequencies with no sign of a low-frequency G' plateau indicating that the system behaved essentially as a liquid, while the value of tan δ decreased with increasing frequency (Figure 8). Within the frequency range that was probed in our experiments, we observed an apparent Winter−Chambon "critical" gel point at $t \approx 56$ min for tan $\delta_c \approx 0.9$, corresponding to $n \approx 0.47$. This value is close to the previously estimated value of $n \approx 0.55$ using microrheology for MAX1 hydrogelation for lower peptide concentrations.[17] For $t > 56$ min, tan δ was lower than its "critical" value (tan $\delta_c \approx 0.9$) for all measured frequencies (Figure 8). The value of tan δ increased with increasing frequency, indicating a possible G' plateau at lower frequencies (G_e') and a possible G', G'' crossover at higher frequencies for $t > 56$ min. A finite G_e' value can be attributed to the permanent nature of cross-links that form the percolating cluster, while the G', G'' crossover frequency can be attributed to local relaxations within clusters due to the stress fields coupled with collective diffusion. G_e' increased further with increasing assembly time for $t > 56$ min, presumably due to essentially permanent cross-links within the clusters and those that form between the percolating cluster and smaller clusters. The

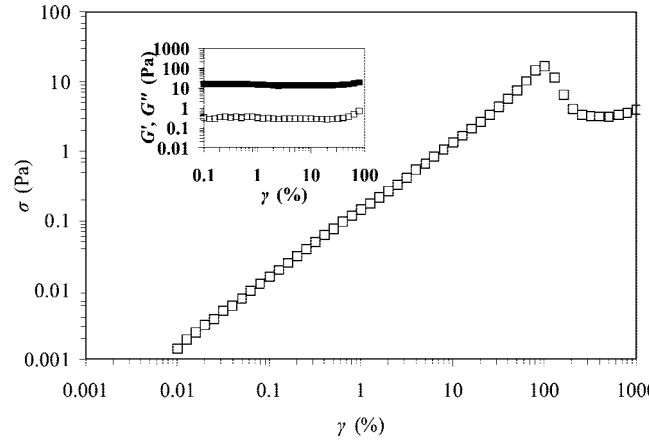

Figure 9. Oscillatory shear stress−strain curve collected at $t = 600$ min. The inset shows the corresponding strain sweep data (G': solid symbols; G'': open symbols).

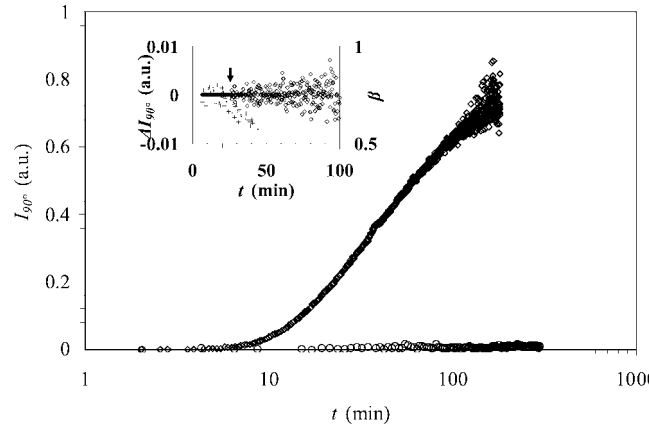

Figure 10. Time evolution of DLS count rates collected at 90° scattering angle for the high salt sample (◇) and low salt control (○). The inset shows the time evolution of intensity fluctuations $\Delta I = (I_{measured}/\langle I\rangle - 1)\langle I\rangle^{0.5}$ (◇) and the β exponent (+) for high salt sample.

increase in G_e' slowed down and G_e' approached a value of $G_{e,\infty}' \approx 20$ Pa at infinite time. At $t \approx 600$ min, the system showed linear viscoelastic behavior up to 100% strain (Figure 9).

3.4. Dynamic Light Scattering. We simultaneously collected DLS detector count rates and autocorrelation functions (ACF) at 90° detector angle ($q = 0.022$ nm^{-1}) after triggering peptide self-assembly. Figure 10 gives typical plots of the detector count rates as a function of assembly time for the same assembly conditions used in the CD, cryo-TEM, and rheology experiments. The count rate for the control peptide solution in low salt buffer ($\kappa^{-1} \approx 1.0$ nm) stayed flat at the buffer solution scattering value, indicating that there was no structural growth due to peptide folding and self-assembly for this assembly condition. On the other hand, when peptide folding and self-assembly were triggered by increasing the solution ionic strength using the high salt buffer ($\kappa^{-1} \approx 0.5$ nm), the count rate increased sigmoidally. An increase in scattered intensity fluctuations formed after $t \approx 26$ min (Figure 10 inset), indicating the possible onset of intercluster interactions.[29,39,40]

We followed the temporal evolution of the distribution of relaxation times $G(\tau_R)$ (for $q = 0.022$ nm^{-1}) using CONTIN analysis (Figure 11). These relaxation times (τ_R) were converted into apparent hydrodynamic correlation lengths, $\zeta = kT\tau_R q^2/6\pi\eta$ (k is the Boltzmann constant, T is the absolute temperature, τ_R is the relaxation time at the scattering vector q, and η is the

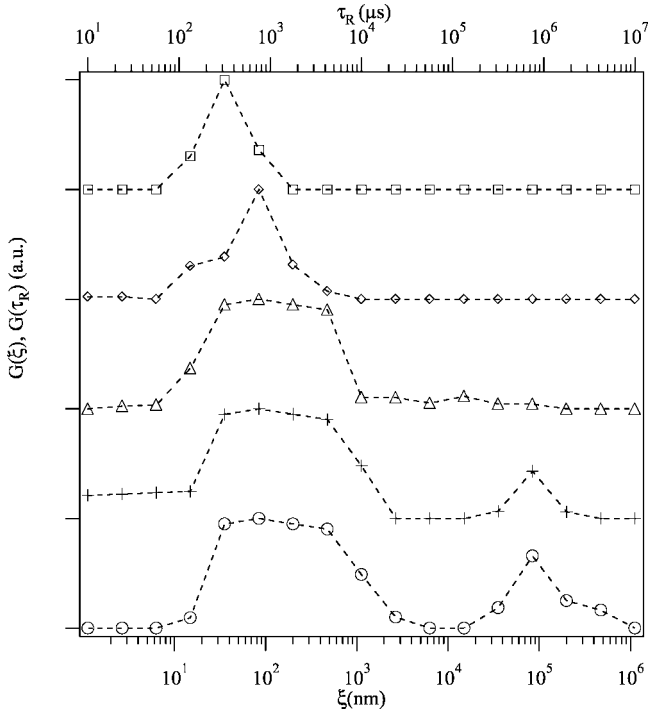

Figure 11. CONTIN dynamic correlation length (bottom x-axis) and relaxation time ($q = 0.022$ nm^{-1}, top x-axis) distributions obtained at different stages of self-assembly: (□) $t = 12$ min, (◇) $t = 26$ min, (Δ) $t = 56$ min, (+) $t = 63$ min, and (○) $t = 160$ min. The quality of the CONTIN fits to the autocorrelation function data is shown in Figure SI-2.

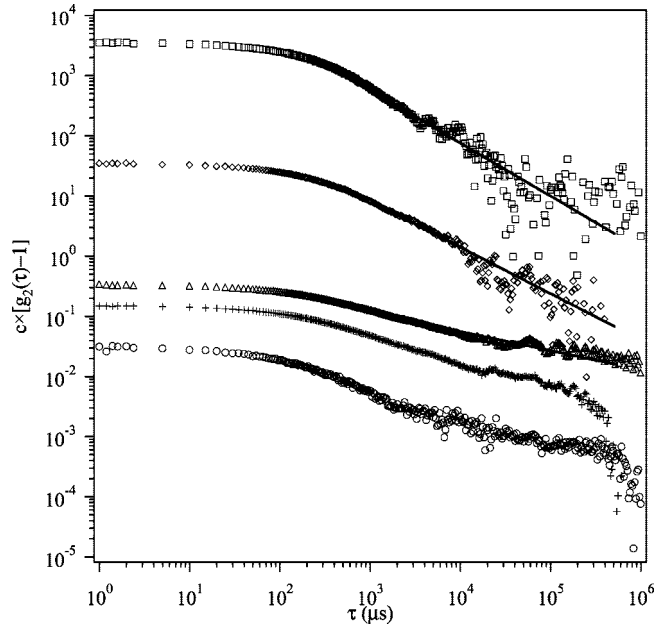

Figure 12. DLS ACF data after gelation (lines show the power law fits to ergodic data): (□) $t = 56$ min ($c = 10^4$), (◇) $t = 63$ min ($c = 10^2$), (Δ) $t = 160$ min ($c = 10^0$), (+) $t = 264$ min ($c = 10^0$), and (○) $t = 1314$ min ($c = 10^0$) where c is an arbitrary shift factor used for easy visualization of multiple ACF data.

solvent viscosity), to eliminate the q dependence. Figure 11 shows the time evolution of the distribution of the dynamic correlation lengths, $G(\xi)$, and that of the relaxation times, $G(\tau_R)$. Immediately after the apparent lag phase in the count rates ($t \approx 12$ min), the main relaxation mode spanned from $\tau_R \approx 0.1-1$ ms, which corresponded to hydrodynamic correlation lengths $\xi \approx 10-100$ nm. This mode could be attributed to a combination of collective diffusion[41–43] relating to the diffusive motion of both fibrils inside the clusters that define the cluster mesh size and to cluster self-diffusion. At $t \approx 26$ min, the distribution shifted to longer times and broadened, presumably due to cluster growth: $\tau_R \approx 0.1-10$ ms ($\xi \approx 10$ nm-1 μm). The broadening of the relaxation time distribution was clearly observed by a simultaneous decrease in the β exponent of the stretched-exponential model (eq 2) (Figure 10 inset). Importantly, $t \approx 26$ min was also when increased fluctuations in the scattered intensity appeared as mentioned above. However, there was no decrease in the initial amplitude of the ACF at this stage; the system was ergodic, and the Siegert relationship (eq 1) was still valid. Broadening of the distribution could be due to diffusion of clusters that are larger than the correlation length and intercluster separations being probed by the relaxation distribution.[41] Both the increased scattered intensity fluctuations and broadening of the relaxation distribution indicated an onset of intercluster interactions in solution.

At $t \approx 56$ min, the onset of a very slow mode was discernible as a small, broad peak at $\tau_R \approx 0.1-10$ s (Figure 11). We attributed this mode to formation of a percolating cluster and the resulting viscoelastic behavior due to gelation. The amplitude of the gel mode gradually increased for $t > 56$ min (this mode becomes clearly noticeable at $t \approx 63$ min), indicating increasing viscoelastic contribution. Power law decay of the ACF was reported for many physical and chemical gels at the gelation threshold (time-averaged ACF $g_2(\tau_R) - 1 \propto \tau_R^{-\mu}$, with critical power law exponents, μ, between 0.39 and 0.9)[29,39–41,44] even though an exact relationship between this power law exponent and that obtained by rheology was highly debated.[40,45] A power law fit to the time−intensity ACF at $t \approx 56$ min gave a power law exponent, $\mu \approx 0.9$ (standard deviation, $\sigma = 0.014$) from 1 ms to 1 s (Figure 12). We also observed apparent power law decay after gelation, while the μ exponent progressively decreased ($\mu \approx 0.4$ at $t \approx 160$ min). There was a noticeable decrease in the initial amplitude of the ACF for $t > 160$ min. This indicated that the gel mode dominated over other slow, ergodic modes for $t > 160$ min and there was a gradual increase in frozen intensity fluctuations.

4. Discussion

The results obtained by CD, cryo-TEM, DLS, and rheology techniques for the same peptide under the same assembly condition at the same time points were combined to obtain a complete picture of early time MAX1 self-assembly and hydrogelation.

4.1. Formation of a Percolated Network. Cryo-TEM data indicated that intramolecularly folded β-hairpins self-assembled into branched clusters of well-defined nanofibrils. At $t \approx 26$ min, when the extent of β-sheet content calculated from the CD signal $X_A \approx 0.5$ (Figure 13a), the hydrodynamic correlation length distribution obtained by DLS broadened distinctly. Simultaneously, increased scattered intensity fluctuations were observed by DLS, indicating an onset of interactions between growing pregel clusters (Figure 13b). Cryo-TEM indicated that such early stage intercluster interactions were possible in solution through dangling fibrils that extended from one cluster to another. However, these early stage interactions between clusters did not contribute significantly to the mechanical response as measured by rheology. In fact, intercluster interactions only affected the stress response of the peptide system at later stages of self-assembly (vide infra), which may partially be attributed to the branched nature of the fibril clusters. It has been suggested in the literature that a higher concentration of intercluster entanglements may be required to affect the dynamics of branched polymeric chains in contrast to a pronounced

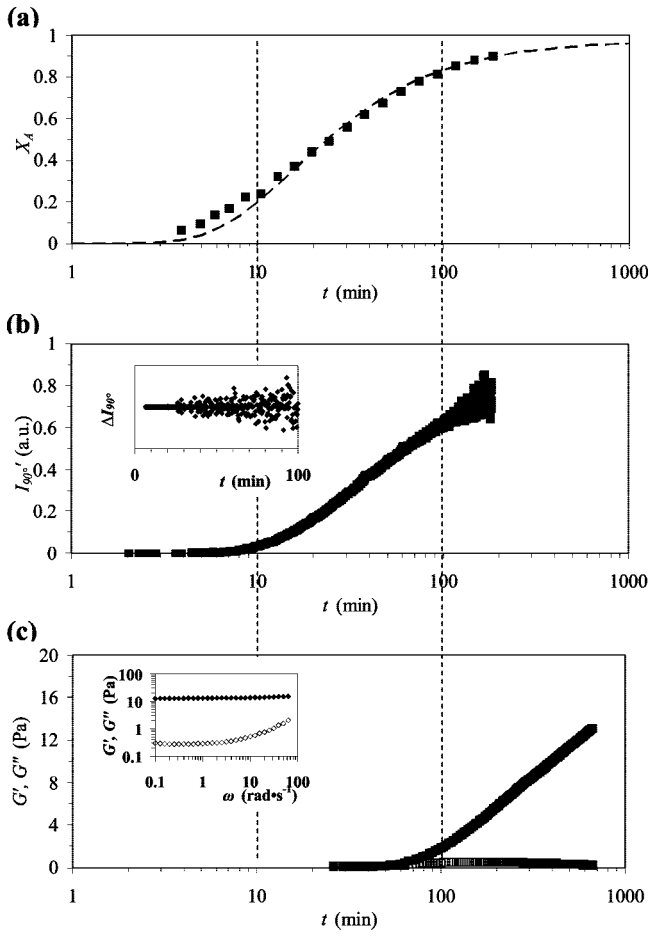

Figure 13. Correlation between (a) the extent of assembly measured by CD, (b) DLS count rates, and (c) rheology time sweep data for $\omega = 1$ rad s^{-1} for the high salt sample (G': solid symbols; G'': open symbols). The inset in (b) shows speckle pattern formation for high salt sample at $t \approx 26$ min. The inset in (c) shows frequency sweep data for 0.25 wt %, high salt sample at $t = 600$ min.

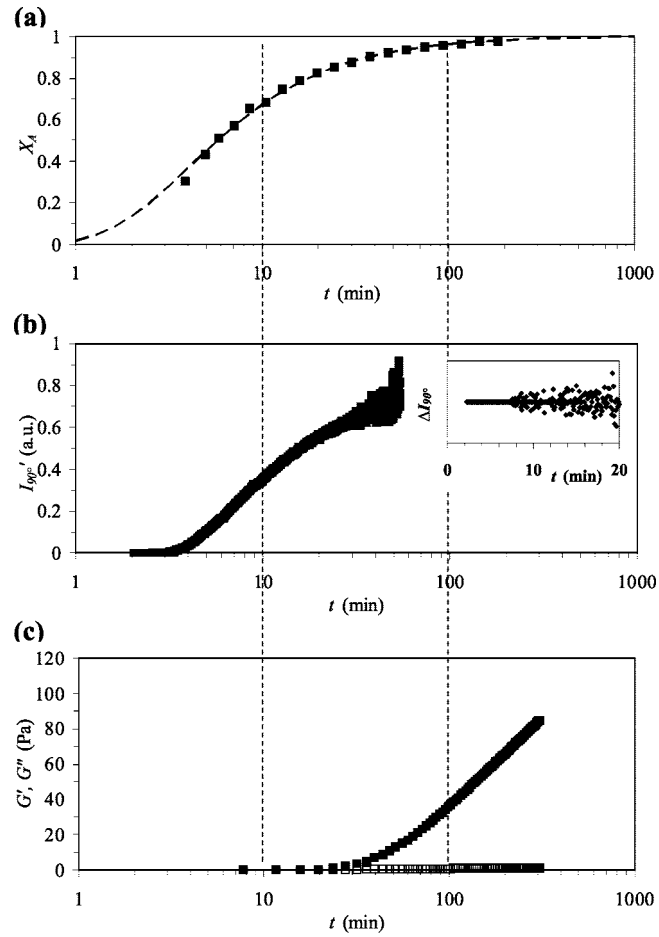

Figure 14. Correlation between (a) the extent of assembly measured by CD, (b) DLS count rates, and (c) rheology time sweep data for $\omega = 1$ rad s^{-1} for the 0.5 wt %, high salt sample (G': solid symbols; G'': open symbols). The inset in (b) shows speckle pattern formation for the 0.5 wt %, high salt sample at $t \approx 7$ min.

change expected for linear, unbranched chains due to interchain interactions at the dilute to semidilute transition.[22,23]

At $t \approx 45$ min, clusters extending over several micrometers were observed by cryo-TEM, in good agreement with the hydrodynamic correlation lengths calculated by DLS, suggesting an approach to gelation. At $t \approx 56$ min, when $X_A \approx 0.75$, both DLS and rheology indicated a possible gelation threshold. A viscoelastic, slow mode appeared in the relaxation time distributions obtained by DLS, while the ACF showed power law behavior with $\mu \approx 0.9$. Rheology data at $t \approx 56$ min suggested a critical dynamic exponent, $n \approx 0.47$. According to simulations by Muthukumar and Winter,[46] $n \approx 0.5$ would correspond to a percolating cluster fractal dimension $D \approx 2$ when hydrodynamic interactions are completely screened and to $D > 2$ in case of partial screening of excluded volume effects.[47] Doi and Onuki obtained equal values of n and β' in polymer solutions and blends[45] where β' is the power law exponent for the field-average autocorrelation function $g(\tau_R) - 1 \propto \tau_R^{-\beta}$ and $\beta' = \mu/2$ according to the Siegert relation (eq 1). They attributed the equality between n and β' to the dynamic coupling between stress and composition. This relationship seems to hold in MAX1 hydrogelation ($n \approx 0.47$, $\beta' \approx 0.45$) and suggests that both rheology and DLS probe the same, self-similar, percolating gel at percolation. After the apparent percolation, the power law behavior was perturbed initially at larger length scales as probed by rheology as a G' upturn in the low-frequency regime, indicating finite interpenetration of the percolating gel and smaller clusters. The subsequent increase in network stiffness for $t > 56$ min (Figure 13c) indicates the formation of more permanent intercluster entanglements due to increased intercluster interpenetration and dangling fibril entanglement.

4.2. How General Is the Proposed Hydrogelation Mechanism for MAX1 Self-Assembly? One might ask if the nanostructural growth and hydrogelation mechanism that is proposed in this paper is universal for MAX1. In other words, how would differences in the assembly kinetics, due to differences in the assembly conditions, affect the proposed hydrogelation mechanism that essentially consists of two distinct time scales: one due to early time, dynamic intercluster interactions in solution and the second due to a percolation-like transition? To address this question of universality, we investigated the time evolution of self-assembled nanostructure and the hydrogelation kinetics under the same solution condition termed as "high salt" in this paper, except with twice the concentration of the MAX1 peptide (0.5 wt % MAX1, pH 7.0, 50 mM bis-tris propane buffer with 0.4 M NaCl salt at 22 °C) using CD, DLS, and rheology (Figure 14). Under these assembly conditions we still observed two distinct time scales, one of which was presumably due to intercluster communication in solution and the other due to gelation, similar to those observed in the lower peptide concentration sample, 0.25 wt % MAX1. However, both thresholds shifted to shorter times in the case of 0.5 wt % MAX1 as compared to the lower peptide concentration. DLS indicated increased intensity fluctuations at $t_f \sim 7$ min while rheology data collected at an angular frequency of 1 rad s^{-1} indicated that the apparent gelation transition was

at $t_g \sim 15$ min, as observed from the $G'-G''$ cross-over, for 0.5 wt % MAX1 (corresponding t_f and t_g values were ~26 min and ~56 min, respectively, for 0.25 wt % MAX1). Interestingly, the extents of assembly measured by CD corresponding to early-time, intercluster interactions and the percolation-like, gelation transition for 0.5 wt % MAX1 were similar to those obtained under the lower peptide concentration of 0.25 wt % MAX1. The increase in scattered intensity fluctuations due to intercluster interactions was observed when $X_{A,f} \sim 0.6$, and the apparent gelation transition was observed when $X_{A,g} \sim 0.8$ for 0.5 wt % MAX1 (corresponding $X_{A,f}$ and $X_{A,g}$ values were ~0.5 and ~0.75 for 0.25 wt % MAX1). These data support earlier results of Veerman et al.,[17] which suggested peptide concentration-independent $X_{A,g}$ for MAX1 at lower peptide concentrations than those used here. Moreover, Ozbas et al.[11] previously reported $X_{A,g}$ values similar to our current findings under much faster MAX1 self-assembly conditions. Therefore, the nanostructural growth and hydrogelation mechanism proposed in this paper seems to be rather general for MAX1 self-assembly under different assembly conditions, including those that were published earlier.

Interestingly, the local nanostructure of the final hydrogel was generally very similar regardless of differences in assembly conditions and assembly kinetics. As an example, the cryo-TEM image collected from the high salt, 0.25 wt % sample at $t \sim 45$ min (Figure 4g) can be compared to the network nanostructure observed in the cryo-TEM image in Figure 1b collected from a MAX1 gel formed under much faster assembly conditions (1 wt % MAX1 hydrogel in pH 9 borate buffer at 40 °C), which effectively induced gelation within the first minute after self-assembly was triggered. Both images show the same nanofibrillar morphology with monodisperse fibril cross section and the two types of proposed cross-links, i.e., defect-induced cross-links and entanglements, in the length scales probed by cryo-TEM.

4.3. Intramolecular Folding Controlled Self-Assembly Kinetics. CD data indicated that the forces dictating self-assembly operate in subnanometer length scales (0.5−1 nm). Both CD and DLS signals (Figure 13, a and b, respectively) display a similar sigmoidal shape. CD signal detects the increase in β-sheet content due to both intramolecular folding and intermolecular self-assembly. Scattered intensity in DLS is mainly influenced by intermolecular self-assembly events since these events lead to the apparent molecular weight increase. The similarity between CD and DLS signals indicates that the kinetics of self-assembly is controlled by intramolecular folding events and that intramolecular peptide folding and intermolecular self-assembly happen essentially concurrently. As a result, large, branched, self-assembled fibril clusters appear immediately after the peptide folding is triggered as observed by cryo-TEM data.

5. Conclusions

In this paper, we report a direct observation of nanostructure evolution correlated with changes in peptide molecular conformation and hydrogel viscoelastic properties. We demonstrate that a complete picture of the self-assembly mechanism, from molecular scale through final material properties characterization, can be obtained only through the combination of several experimental techniques. Combined data indicate two distinct time scales for the formation of the hydrogel scaffold: (1) early time fibril cluster formation and intercluster overlap through dangling fibrils and (2) percolation of clusters of nanofibrils. The knowledge of these two time scales may provide a new strategy for the 3-d, homogeneous encapsulation of cells in the hydrogel scaffold for tissue regeneration applications.[16] Previously in Haines-Butterick et al.,[16] favorable assembly kinetics for homogeneous cell encapsulation were achieved through peptide design. Specifically, a point amino acid substitution was made on the hydrophilic face of MAX1 peptide by replacing the lysine residue at position 15 with a glutamic acid. This substitution resulted in a change of −2 in the overall peptide charge state. Consequently, the electrostatic forces impeding peptide intramolecular folding were reduced relative to the parent MAX1 peptide and faster assembly kinetics were achieved in cell culture medium. As a result, the fast assembly kinetics prevented the sedimentation of cells and enabled the homogeneous encapsulation of the cells in three dimensions. However, depending on the specific tissue regeneration application, one might desire a specific peptide primary structure that inherently affords slow assembly kinetics and, thus, does not provide homogeneous cell encapsulation based on the fast kinetic trapping of the cells. An alternative strategy for the homogeneous encapsulation of cells that essentially divorces cell encapsulation from fast assembly kinetics is made possible by the knowledge of the early time peptide assembly presented herein. Specifically, it may be possible to introduce cells in the self-assembling system sometime between the onset of intercluster interactions and cluster percolation. This timing of cell introduction could lead to the immediate encapsulation of the added cells due to the quick transition from a liquid suspension of fibril clusters to a percolated network. Thus, one could kinetically trap cells in a percolated network that underwent slow assembly kinetics in cell culture medium.

Structural characteristics, such as monodisperse fibril dimensions, and the branching mechanism are clearly different from those reported for biopolymeric systems in the literature. The former implies high prospects for future bioengineering applications, while both characteristics should be considered when describing the viscoelastic properties of the network as well as a future complete kinetic model for MAX1 assembly.

Acknowledgment. This work was supported by National Institutes of Health (Grant 5R01DE016386-04). We thank National Center for Neutron Research at the National Institute of Standards and Technology for SANS beam time and the W. M. Keck Foundation for funding the College of Engineering Electron Microscopy Laboratory. We thank Congqi Yan for her help with rheology experiments, Dr. Chao Ni and Frank Kriss for their help with TEM experiments, and Dr. Robert Prud'homme, Dr. George Fytas, Dr. Boualem Hammouda, and Dr. Eric Furst for inspirational and insightful scientific conversations.

Supporting Information Available: Time evolution of storage modulus for 0.25 wt %, high salt assembly condition at different strain amplitudes (Figure SI-1) and quality of CONTIN fits to autocorrelation function data from which hydrodynamic correlation lengths in Figure 11 were obtained (Figure SI-2). This material is available free of charge via the Internet at http://pubs.acs.org.

Note Added After ASAP Publication. This article was published ASAP on July 1, 2008. The content of ref 21 has been changed. The correct version was published on July 18, 2008.

References and Notes

(1) Rajagopal, K.; Schneider, J. P. *Curr. Opin. Struct. Biol.* **2004**, *14*, 480–486.
(2) Lee, K. Y.; Mooney, D. J. *Chem. Rev.* **2001**, *101* (7), 1869–1879.
(3) Lutolf, M. P.; Hubbell, J. A. *Nat. Biotechnol.* **2005**, *23* (1), 47–55.
(4) Beebe, D. J.; Moore, J. S.; Bauer, J. M.; Yu, Q.; Liu, R. H.; Devadoss, C.; Jo, B. H. *Nature (London)* **2000**, *404* (6778), 588–590.
(5) Eddington, D. T.; Beebe, D. J. *Adv. Drug Delivery Rev.* **2004**, *56* (2), 199–210.
(6) Peppas, N. A.; Bures, P.; Leobandung, W.; Ichikawa, H. *Eur. J. Pharm. Biopharm.* **2000**, *50* (1), 27–46.
(7) Hoffmann, A. S. *Adv. Drug Delivery Rev.* **2002**, *54*, 3–12.

(8) Langer, R.; Peppas, N. A. *AIChE J.* **2003**, *49* (12), 2990–3006.
(9) Schneider, J. P.; Pochan, D. J.; Ozbas, B.; Rajagopal, K.; Pakstis, L.; Kretsinger, J. *J. Am. Chem. Soc.* **2002**, *124* (50), 15030–15037.
(10) Pochan, D. J.; Schneider, J. P.; Kretsinger, J.; Ozbas, B.; Rajagopal, K.; Haines, L. *J. Am. Chem. Soc.* **2003**, *125* (39), 11802–11803.
(11) Ozbas, B.; Kretsinger, J.; Rajagopal, K.; Schneider, J. P.; Pochan, D. J. *Macromolecules* **2004**, *37* (19), 7331–7337.
(12) Ozbas, B.; Rajagopal, K.; Schneider, J. P.; Pochan, D. J. *Phys. Rev. Lett.* **2004**, *93*, 268106.
(13) Ozbas, B.; Schneider, J. P.; Pochan, D. J. Hydrogels Constructed via Beta-Hairpin Peptide Self-Assembly. *ACS Symp. Ser.* **2006**, *935*, 284–297.
(14) Haines, L. A.; Rajagopal, K.; Ozbas, B.; Salick, D. A.; Pochan, D. J.; Schneider, J. P. *J. Am. Chem. Soc.* **2005**, *127* (48), 17025–17029.
(15) Kretsinger, J. K.; Haines, L. A.; Ozbas, B.; Pochan, D. J.; Schneider, J. P. *Biomaterials* **2005**, *26* (25), 5177–5186.
(16) Haines-Butterick, L.; Rajagopal, K.; Branco, M.; Salick, D.; Rughani, R.; Pilarz, M.; Lamm, M. S.; Pochan, D. J.; Schneider, J. P. *Proc. Natl. Acad. Sci. U.S.A.* **2007**, *104* (19), 7791–7796.
(17) Veerman, C.; Rajagopal, K.; Palla, C. S.; Pochan, D. J.; Schneider, J. P.; Furst, E. M. *Macromolecules* **2006**, *39* (19), 6608–6614.
(18) Samuel, R. E.; Salmon, E. D.; Briehl, R. W. *Nature (London)* **1990**, *345*, 833–835.
(19) Forgacs, G.; Newman, S. A.; Hinner, B.; Maier, C. W.; Sackmann, E. *Biophys. J.* **2003**, *84*, 1272–1280.
(20) Ferrone, F. A.; Hofrichter, J.; Eaton, W. A. *J. Mol. Biol.* **1985**, *183* (4), 611–631.
(21) Van Workum, K.; Douglas, J. F. *Phys. Rev. E* **2005**, *71* (3), 031502.
(22) de Gennes, P. G. *Scaling Concepts in Polymer Physics*; Cornell University Press: Ithaca, NY, 1979.
(23) Cates, M. E. *Philos. Trans. R. Soc. London, A* **1993**, *344* (1672), 339–356.
(24) Tlusty, T.; Safran, S. A. *Science* **2000**, *290* (5495), 1328–1331.
(25) Israelachvili, J. *Intermolecular and Surface Forces*, 2nd ed.; Academic Press Ltd.: San Diego, 1991. The Debye−Huckel screening length (κ^{-1}) was calculated from $\kappa^{-1} = [(N_A e^2/\epsilon\epsilon_0 k_B T)\sum_i(c_i z_i^2)]^{-1/2}$ (m), where N_A is Avagadro's number (mol^{-1}), e is the elementary charge (C), ϵ is the dielectric constant of water, ϵ_0 is the permittivity of vacuum ($C^2\ J^{-1}\ m^{-1}$), k_B is the Boltzmann constant ($J\ K^{-1}$), T is the absolute temperature (K), c_i and z_i are the bulk concentration ($mol\ m^{-3}$) and valency of ion i, and the summation is over all ions in solution. The bulk concentration of Na^+ and Cl^- ions was calculated assuming complete dissociation of the NaCl salt. For bis-tris propane buffer, the concentration of the divalent (H_2L^{2+}) and the monovalent ions (HL^+) in solution were calculated by taking the equilibrium constant (pK) for the first ionization reaction ($H_2L^{2+} = HL^+ + H^+$) as pK = 6.65 (at 25 °C), where L = $C_{11}H_{26}N_2O_6$.
(26) Guinier, A.; Fournet, G. *Small Angle Scattering of X-Rays*; J. Wiley: New York, 1955.
(27) Burkoth, T. S.; Benzinger, T. L. S.; Urban, V.; Morgan, D. M.; Gregory, D. M.; Thiyagarajan, P.; Botto, R. E.; Meredith, S. C.; Lynn, D. G. *J. Am. Chem. Soc.* **2000**, *122* (33), 7883–7889.
(28) Siegert, A. J. F. *Mass. Inst. Technol. Rad. Lab. Rep.* **1943**, *465*, 1–14.
(29) Geissler, E. Dynamic Light Scattering from Polymer Gels. In *Dynamic Light Scattering*; Brown, W., Ed.; Clarendon Press: Oxford, 1993; pp 471–511.
(30) Provencher, S. W. *Comput. Phys. Commun.* **1982**, *27* (3), 229–242.
(31) Stepanek, P. Data Analysis in Dynamic Light Scattering. In *Dynamic Light Scattering*; Brown, W., Ed.; Clarendon Press: Oxford, 1993; pp 177–240.
(32) Talmon, Y. *Colloids Surf.* **1986**, *19* (2−3), 237–248.
(33) Bellare, J. R.; Davis, H. T.; Scriven, L. E.; Talmon, Y. *J. Electron Microsc. Tech.* **1988**, *10* (1), 87–111.
(34) Cui, H. G.; Hodgdon, T. K.; Kaler, E. W.; Abezgaous, L.; Danino, D.; Lubovski, M.; Talmon, Y.; Pochan, D. J. *Soft Matter* **2007**, *3*, 945–955.
(35) Danino, D.; Talmon, Y.; Levy, H.; Beinert, G.; Zana, R. *Science* **1995**, *269* (5229), 1420–1421.
(36) Lin, Z. *Langmuir* **1996**, *12* (7), 1729–1737.
(37) Pouzot, M.; Nicolai, T.; Visschers, R. W.; Weijers, M. *Food Hydrocolloids* **2005**, *19* (2), 231–238.
(38) Chambon, F.; Winter, H. H. *Polym. Bull.* **1985**, *13* (6), 499–503.
(39) Richter, S.; Matzker, R.; Schroter, K. *Macromol. Rapid Commun.* **2005**, *26* (20), 1626–1632.
(40) Shibayama, M.; Norisuye, T. *Bull. Chem. Soc. Jpn.* **2002**, *75* (4), 641–659.
(41) Martin, J. E.; Wilcoxon, J.; Odinek, J. *Phys. Rev. A* **1991**, *43* (2), 858–872.
(42) Ren, S. Z.; Shi, W. F.; Zhang, W. B.; Sorensen, C. M. *Phys. Rev. A* **1992**, *45* (4), 2416–2422.
(43) Ikkai, F.; Shibayama, M. *Phys. Rev. Lett.* **1999**, *82* (24), 4946–4949.
(44) Coviello, T.; Burchard, W. *Macromolecules* **1992**, *25* (2), 1011–1012.
(45) Doi, M.; Onuki, A. *J. Phys. II* **1992**, *2* (8), 1631–1656.
(46) Muthukumar, M.; Winter, H. H. *Macromolecules* **1986**, *19* (4), 1284–1285.
(47) Winter, H. H.; Mours, M. Rheology of polymers near liquid-solid transitions. In *Neutron Spin Echo Spectroscopy Viscoelasticity Rheology*; Springer-Verlag: Berlin, 1997; Vol. *134*, pp 165−234.

MA702840Q